Nanotechnology Perceptions
ISSN 1660-6795
www.nano-ntp.com

Oxide Based Composite for Selective Separation of Oxygen from the Atmospheric Air

Mohammad Adnan Iqbal, Abdur Rahman Quaff

Department of Civil Engineering, National Institute of Technology Patna, Bihar, 80005, India
Email: mdi.phd20.ce@nitp.ac.in

In this study of oxide-based composites for oxygen separation from atmospheric air, focusing on the comparison of oxygen permeability efficiency between perovskite and its composite materials, namely LSCF (lanthanum strontium cobalt ferrite) and LSCF-GDC (lanthanum strontium cobalt ferrite & GDC composite). The research delves into the critical role of oxygen permeation in various applications, such as gas separation technologies and oxygen-enriched air production. Perovskite structures, known for their oxygen ion conductivity, are compared with LSCF and LSCF-GDC composite to assess their effectiveness in facilitating oxygen transport through solid-state membranes. Experimental analyses include measuring oxygen permeability rates under different operating conditions and characterizing the micro structural properties of composite materials. The study aims to elucidate the factors influencing oxygen permeability, including composition, crystal structure, and do pant elements, and to identify the most promising material for efficient oxygen separation. Insights gained from this research can contribute to the development of advanced oxygen separation membranes with improved performance and reliability, addressing challenges in energy-efficient oxygen production and environmental sustainability.

Keywords: Oxide-based composites, Lanthanum strontium cobalt ferrite, Lanthanum strontium cobalt ferrite & GDC composite.

1. Introduction

For industrial and environmental activities, it is crucial to produce oxygen from air separation at a reasonable cost since oxygen is essential for increasing the combustion efficiency of clean energy projects that control CO_2 (Wu et al., 2018). By stopping the wide-scale emissions of CO_2 into the atmosphere from major point sources such as coal power stations, carbon capture and storage has been acknowledging as the most practical technique to combat climate change (Gur et al., 2022). Through the waste gas from modern power plants that use air as an oxidant only contains 12-15% CO_2, obtaining the highly purified CO_2 in an economical way is

necessity for this goal. The primary waste gas generated by industry would be highly refined CO_2, which is easily collected for further storage, if pure oxygen were utilized throughout the combustion process rather than air (Goren et al., 2024). In this case, the oxygen production and the economics of renewable energy initiatives are tightly tied. The large-scale O_2 manufacturing that is currently done on a massive scale using pressure adsorption or traditional cryogenic processes is costly and energy-intensive (Bahrun et al., 2022).

2. Experimental Section

2.1 Material Section

$La(NO_3)_3.6H_2O$, $Sr(NO_3)_2$, $Co(NO_3)_2.6H_2O$ and $Fe(NO_3)_3.9H_2O$ are the metallic nitrates; ammonium solution, EDTA acid, citric acid, an ammonium nitrate, which were supplied by Merck Co. with a purity of higher than 99.9% , are required materials for the synthesis of $La_{0.6}Sr_{0.4}Co_{0.2}Fe_{0.8}O_{3-\delta}$ (LSCF) powder.

2.1.1 Preparation of LSCF Powder

The needed quantity of EDTA acid is dissolved in an ammonium solution to create the $La_{0.6}Sr_{0.4}Co_{0.2}Fe_{0.8}O_{3-\delta}$ membranes by autocombustion. Then, in order to create a metal nitrate solution, the stoichiometric quantities of each metal nitrate are individually dissolved in deionized water and then combined. Next, this solution is mixed with citric acid added. Total metallic cations, citric acid, and EDTA acid are all mixed in 1:2:1 molar ratio. The combined solution is mixed with the required amount of NH_4NO_3 in the fourth stage. Next by adding the necessary amount of ammonium solution, the pH of the mixture is adjusted to six. It is appropriate to note that the combination of citric acid, EDTA, and ammonia results in a buffer solution with a pH that is very that is very near to 6. The four metallic cations in the solutions are stabilized as a result of the chelating action of EDTA and citric acid. It is possible to link with a metallic atom through any of these two chelating agent's electron donor atoms and prevent the metal cations from partially segregating. After roughly five hours, a gel is produced while the mixture is agitated over a hot plate at 90℃. An ammonia solution is added to the solution to maintain a pH of 6 throughout the stirring time. The resulting gel is then moved to an autocombustion process-ready furnace that has been warmed to 250℃. Equation 1 summarizes the autocombustion reaction. There is no doubt that this process uses up oxygen. The oxygen line is attached to the furnace to facilitate the entire combustion process.

$$0.6La(NO_3)_3 + 0.4\,Sr(NO_3)_2 + 0.2Co(NO_3)_2 + 0.8Fe(NO_3)_3 + 2C_{10}H_{16}N_2O_8 + 4C_6H_8O_7 + 25NH_4NO_3 + \frac{1}{2}(37.8-\delta)O_2$$

$$La_{0.6}Sr_{0.4}Co_{0.2}Fe_{0.8}O_{3-\delta} + 29.7N_2 + 82H_2O + 44Co_2 \qquad (2)$$

The extremely fine and porous powder is then transferred to an alumina crucible and heated at 1000℃ for five hours under static air at heating and cooling rates of 1℃/min after the furnace has been cooled to room temperature at a rate of 1℃/min. After the organic elements are burned out of the powder structure during this calcination process, LSCF perovskite powder is the end product.

2.1.2 Fabrication of the Small circular disc

The LSCF powder weight 0.8740 gm that was achieve had a small circular disc form with a diameter of 12.20 mm and a thickness of 2.77 mm. Finally, in order to achieve the required relative density and gas-tightness, the raw disks were sintered for 8 hours at 1200℃, with heating and cooling rates of 1℃/min. For LSCF powder, these are optimal shape and sintering parameter values that were found.

2.1.4 Characterization of LSCF-6428 powder

Figure 2 shows the x-ray diffraction (XRD) pattern of lanthanum strontium cobalt ferrite (LSCF) powder, which is an important indication of its structural properties. A clear sign that a crystalline single-phase compound has formed is the existence of prominent peaks in the XRD pattern. This demonstrates that the autocombustion method which uses a spontaneous burning mechanism to speed up synthesis was successful in synthesizing LSCF. When organic additives are added to a main powder mixture, they quickly burn throughtout the process, resulting in a bulk product that is extremely porous and has well-separated powder particles. As a result, there is no longer a requirement for a milling process, which removes any possibility of contaminants arising from such mechanical processing.

By utilizing the XRD data, the lattice constant of the LSCF powder may be computed and discovered to be 3.862402 Å. The atomic arrangement and spacing inside the crystalline structure of LSCF are better understood thanks to this measurement of lattice constant. Characterizing the material's characteristics, including its phase composition, crystal structure, and possible uses, is made easier with an accurate measurement of the lattice constant. The successful synthesis of crystalline LSCF is confirmed by the combination of XRD analysis and lattice constant determination, which also provides a deeper understanding of its structural properties and opens up new avenues for research and development in fields like energy conversion and storage systems.

2.2 Preparation of LSCF-GDC composite Powder

In our experimental procedure, we utilized solid-state reaction to prepare the LSCF-GDC composite. The composite powder was prepared with a weight mixing ratio of LSCF to GDC of 50:50. We employed a high-speed attrition-type mill equipped with a stainless-steel chamber and rotor for the synthesis of LSCF–GDC composite particles. Detailed configuration of the mill setup has been previously described.

Initially, commercially available La2O3 (average particle size, dBET = 300 nm), Sr (OH)2 (dBET = 750 nm), Co_3O_4 (dBET = 23 nm), and Fe_2O_3 (dBET = 34 nm) were mixed in stoichiometric quantities totaling 70 g. Additionally, one-fifth of the total amount of GDC powder ($Ce_{0.9}Gd_{0.1}O_{1.95}$, dBET = 24 nm) was included in the chamber. The powders underwent mechanical treatment under ambient air conditions without external heating. A motor (2.7 kW) drove the rotor with a maximum rotation speed of 4500 rpm. During the mechanical processing, one-fifth of the total amount of GDC powder was incrementally added every 4 minutes, spanning a total processing time of 20 minutes.

2.3 Oxygen Permeability Test

The technique for conducting an oxygen permeability test explains how to use a falling head

permeameter for measuring. Because there is a pressure differential between the top (P_{atm}) and lower (P) sides of the sample, the test measure the constant, unidirectional flow of gas through the specimen. The sample is at atmospheric pressure at its top surface, while its bottom surface is in touch with the oxygen inside the vessel at a specified pressure. Measuring the pressure decrease over time allows one to quantify the gas flow. To conduct the test, the sample is put inside the upper cell, secure with a rubber collar, and squeezed to gurantee a tight seal around the edges. After opening the input valves and allowing the gas to pass through the cylinder for a brief amount of time (in seconds), the outlet valve is closed, allowing the relative pressure inside the cylinder to rise to around 100kPa. Four samples are put through testing at the same time.

Under the scenario of compressible gas flow, the oxygen permeability is calculated using D'Arcy's law. The expression for the gas flow per cross sectional area depends on the gravity acceleration (g), the coefficient of permeability ($k_{\delta A}$), and the pressure decay ($\partial P/\partial z$).

$$\frac{\partial m}{\partial t} = -\frac{k_{\delta A}}{g}\frac{\partial p}{\partial z} \qquad (3)$$

Where z is the spatial coordinates that shows the location across the sample in the gas flow's direction. An equation for the assessment of oxygen permeability may be obtained by combining Equation (3) with the ideal gas law (Equation (4)).

$$k_{\delta A} = \frac{\omega v g d}{RAT}\frac{1}{t}\ln\left(\frac{P_0}{P}\right) \qquad (4)$$

Where T is the absolute temperature, 293.15 K, A is the sample's cross-sectional area (m^2), d is its thickness (m), R is the universal gas constant, 8.314 (N m)/(K mol), and ω is the oxygen molecular mass, 0.032 kg/mol. Also, V is the oxygen volume under pressure (m^2). The term $\ln(P_0/P)/t$ has been assessed taking into account a linear regression driven via the origin. Equation (5) represents the estimate $\hat{m}$ of the linear regression slope via ordinary least square.

$$\frac{1}{t}\ln\left(\frac{P_0}{P}\right) \cong \hat{m} \cong \frac{\sum_{t=1}^{n}[\ln\frac{P_0}{P_t}]^2}{\sum_{t=1}^{n}[\ln\frac{P_0}{P_t}]t_t} \qquad (5)$$

P_0 represents the starting pressure, P_i is the pressure at time t_i, and n denotes the total number of data points that is, pressure that are being collected.

The oxygen permeability index (OPI) may be calculated using Equation (6), which takes the logarithm of the average permeability values found in the four tested samples.

$$OPI = -\log_{10}\left(\sum_{t=1}^{A}\frac{k_{SAt}}{4}\right) \qquad (6)$$

where k_{SAt} represents each samples's oxygen permeability as determined by Equation (4).

The coefficient of permeability k_{SA} utilized in this investigation (Equation(4)) is represented in m/s, although the conventional values of gas permeability (k_{cem}) are expressed in m^2. The following equation (Equation(7)) shows how the two formulations are connected by the gas density $\rho(kg\ m^{-2})$, gravity acceleration $g\left(\frac{m}{s^2}\right)$, and dynamic viscosity μ ($N\ s\ m^{-2}$).

$$\frac{k_{SA}}{k_{cem}} = \frac{\rho g}{2\mu} \qquad (7)$$

When the water-to-cement ratio (w/c) is between 0.35 and 0.70, mortar tests typically provide oxygen permeability ranging from 10^{-15}m/s to 10^{-10}m/s. The oxygen permeability values of concrete usually fall between 10^{-13}m/s and 10^{-10}m/s. The variety of findings shown stems from various conditioning techniques (crack presence, degree of saturation and gas connection, ITZ, pore sizes, and connectivity) as well as compositions (porosity, pore sizes, and network connectivity).

3. Results and Discussions

The morphology and microstructure of prepared LSCF & LSCF-GDC composite powder was studied under a field enhanced scanning electron microscope at different magnifications. The FESEM micrographs of LSCF powder show dense microstructure with uniformly distributed grain sizes. The mean grain size is observed to be around 1 micrometre. In case of LSCF-GDC composite powder, the compact microstructure is shown by micrographs due to better sintering. The observed density is close to the theoretical density. Presence of gadolinium has facilitated in the sintering process and resulted in such dense microstructure with uniformly distributed grains of mean size of more than 1 micrometre. The grain size of LSCF-GDC composite powder is larger than the LSCF powder. LSCF powder membrane shows the flowered morphology.

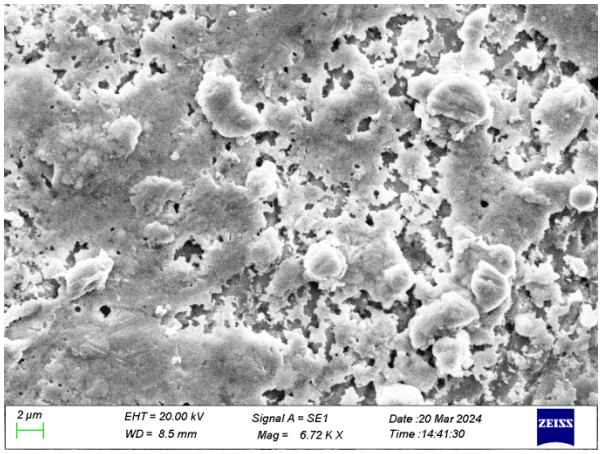

A

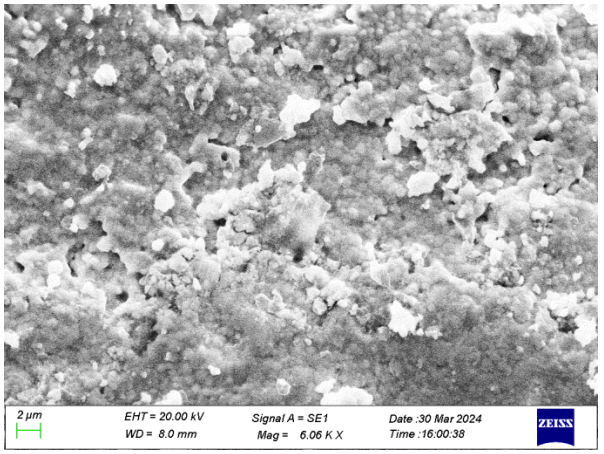

B

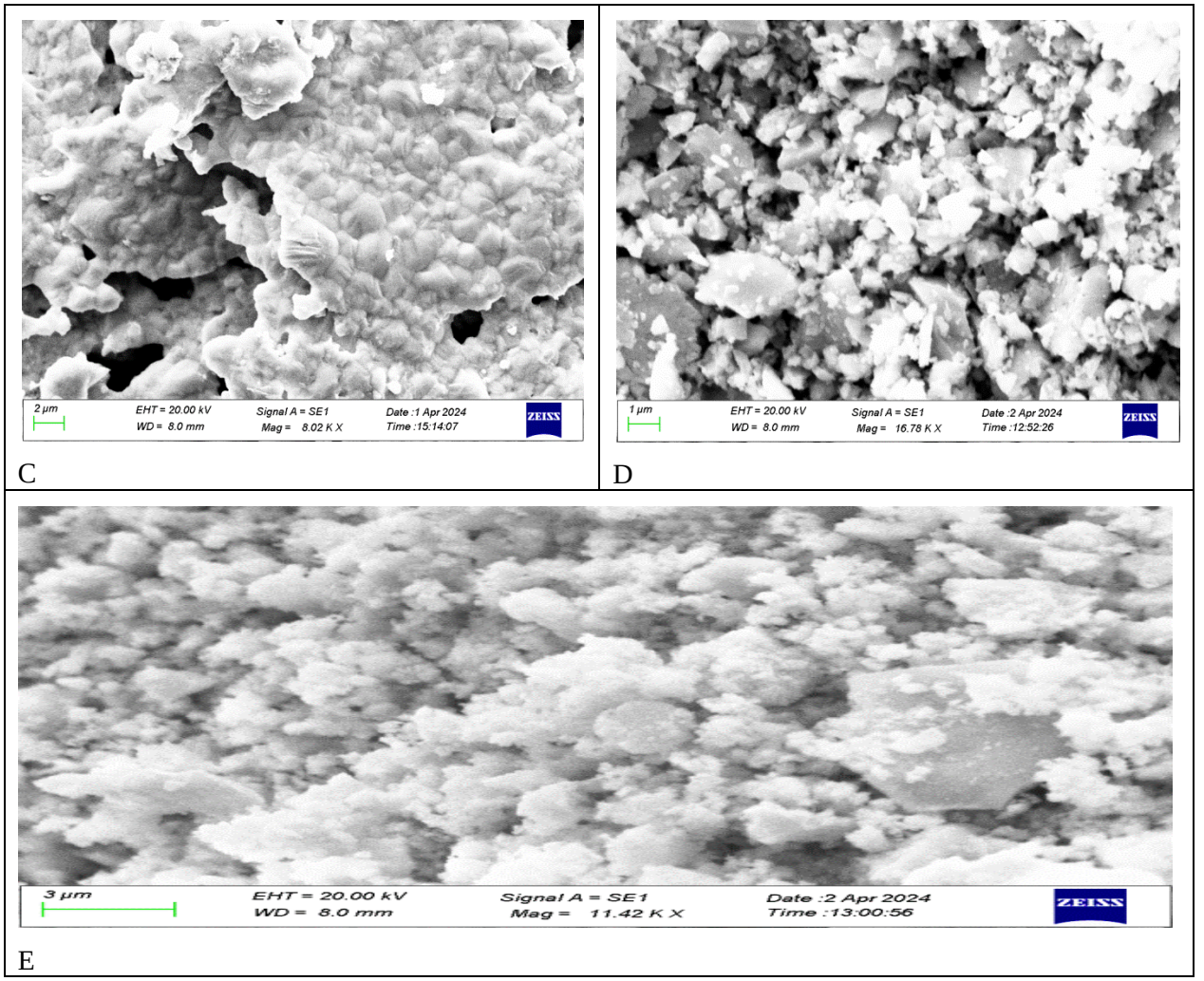

Figure 2: FE-SEM micrographs of (a,b,e) $La_{0.6}Sr_{0.4}Co_{0.2}Fe_{0.8}O_{3-\delta}$ (LSCF) powder and (c,d) LSCF-GDC composite powder.

Variation of dielectric constant with frequency

The dielectric constant measures a material's ability to polarize under an applied electric field. Nano-crystalline spinel ferrites are known for their excellent dielectric properties, influenced by factors such as cation distribution, particle size, and synthesis method. Studies on gadolinium-doped ferrites, conducted by Ahmed and Muthafar, explored the dielectric behaviour across a frequency range of 100Hz to 20MHz at various temperatures.

In general, all compositions exhibited normal dielectric behaviour. The dielectric constant showed a characteristic trend: it decreased with increasing frequency and eventually stabilized at higher frequencies. This behaviour is typical for ferrites and can be explained by models such as Maxwell-Wagner and Koop's theory. These models suggest that ferrites consist of a heterogeneous mix of highly conductive grains separated by less conductive grain boundaries.

At lower frequencies, these boundaries are active, requiring more energy for electron hopping. As frequency increases, more conductive grains are activated, leading to stabilized polarization and a constant dielectric constant.

Variation of dielectric loss with frequency

Dielectric loss (ε") behaviour with frequency is another critical aspect of ferrite systems, particularly gadolinium-doped nickel ferrites. The plots of dielectric loss against frequency typically show a rapid decrease in the low-frequency region, followed by a more gradual decrease to a near-constant level at higher frequencies.

Koop's phenomenological theory provides an explanation for this behaviour. In the figure 3 the low-frequency region, poorly conducting grain boundaries are active, requiring significant energy for electron hopping and thus resulting in higher dielectric losses. As frequency increases, the more conductive grains become dominant, reducing the energy required for electron hopping and resulting in lower dielectric losses.

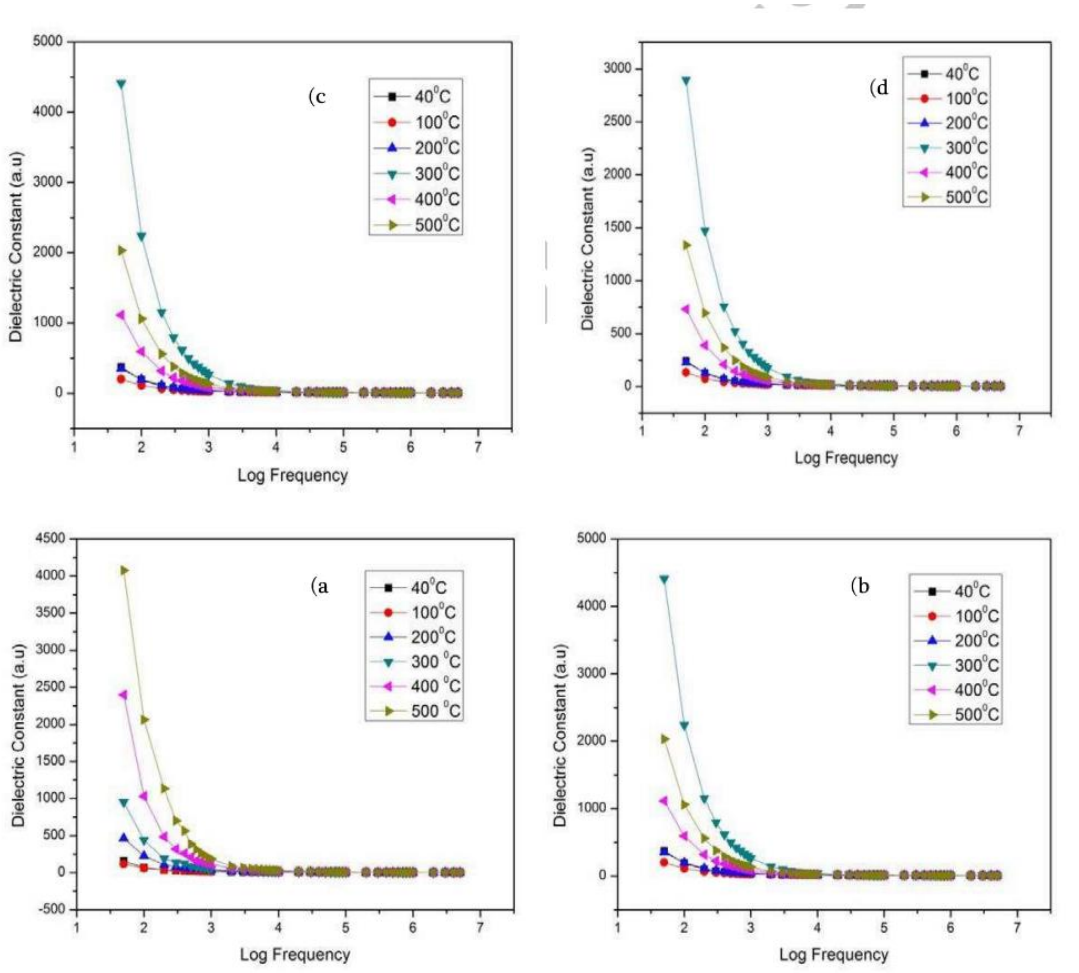

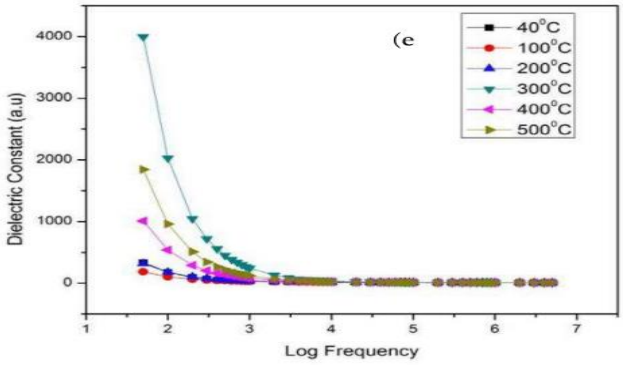

Figure 3: - Variation of dielectric constant with frequency

X-ray photoelectron spectroscopy (XPS)

X-ray photoelectron spectroscopy (XPS) is a surface-sensitive technique that can provide valuable information about the elemental composition and chemical state of the surfaces of materials. In your study, XPS could be used to analyze the perovskite and composite materials (LSCF and LAGF-Gd) to understand:

1. Elemental Composition: XPS can quantify the elemental composition at the surface of the materials, helping to verify the presence and distribution of lanthanum, strontium, cobalt, ferrite, gadolinium, gallium, and oxygen.

2. Chemical States: It can identify the chemical states of elements, such as different oxidation states of transition metals like cobalt and gallium, which can influence oxygen ion conductivity.

3. Surface Structure: XPS can reveal the surface structure and morphology of the materials, providing insights into surface roughness, defects, and chemical bonding configurations.

In the context of our research comparing oxygen permeability efficiency between perovskite and its composites, XPS data would be crucial for understanding how the surface chemistry and composition of the materials affect their oxygen ion conductivity and overall performance as oxygen separation membranes.

Characterization of LSCF Cathodes using XPS

X-ray photoelectron spectroscopy (XPS) is a powerful technique for analyzing the chemical composition near the surface and the oxidation states of elements based on their binding energies. In the study of LSCF cathodes, in situ synchrotron-based XPS has been employed to investigate how strontium (Sr) segregation accelerates degradation mechanisms. This method is particularly sensitive to surface effects, which can limit the surface catalytic activity for oxygen reduction reactions (ORR). Figure below presents typical XPS spectra of the LSCF cathode, highlighting peaks corresponding to LSCF 6428. Liu et al. explored the degradation mechanisms of LSCF and LSCF/GDC composite cathodes under various cathodic current polarizations using XPS.

The observed reduction in surface strontium (Sr) concentration suggests that during high cathodic polarization treatment, Sr is likely being incorporated into the lattice structure of LSCF (lanthanum strontium cobalt ferrite). Despite this incorporation, the La/Sr ratio after the current polarization treatment remains below the stoichiometric ratio of 1.5 required for LSCF.

This phenomenon indicates that even though Sr is migrating into the lattice, the process is not sufficient to achieve or maintain the ideal chemical composition of LSCF. This deviation from stoichiometry can influence the material's properties, including its oxygen ion conductivity and stability, both of which are critical for its performance as a cathode material in solid oxide fuel cells (SOFCs) or other oxygen-related applications.

Understanding these dynamics is essential for optimizing the fabrication and performance of LSCF and similar materials, ensuring they meet the required stoichiometric ratios for optimal functionality in various technological applications. Further research using techniques like in situ synchrotron-based XPS can provide deeper insights into these processes, aiding in the development of more efficient and durable materials for energy conversion and other advanced technologies.

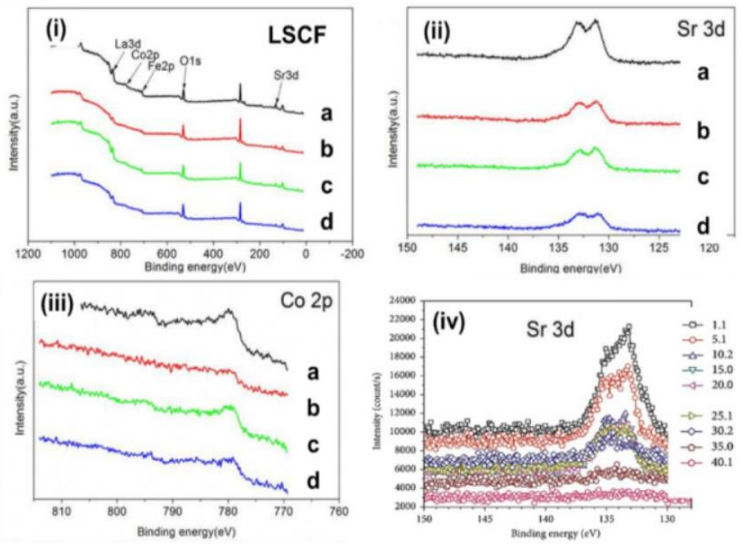

Figure 4:- (i) XPS spectra of LSCF, showing La 3d, Sr 3d, Co 2p, and Fe 2p peaks (ii) magnified image of Sr 3d peak (iii) magnified image Co 2p peak for (a) as-prepared sample, (b) under open circuit at 750 °C in the air for 120 h, (c) polarized sample under 100 mA cm^{-2} at 750 °C for 120 h, and (d) polarized sample under 200 mA cm^{-2} at 750 °C for 120 h. (iv) Sr 3d peaks obtained from XPS depth profile measurements at different depths in micrometers.

Initially, the XPS spectra of the raw LSCF powder served as a baseline, offering insights into the initial composition and surface state of the material before electrode preparation. The freshly prepared LSCF electrode spectra were then examined to understand the immediate surface changes induced during electrode fabrication. Subsequently, the LSCF electrode annealed for 24 hours was analyzed to assess the structural and compositional alterations

following thermal treatment, which is crucial for stabilizing the perovskite structure and potentially inducing phase transformations or surface segregation phenomena.

Moreover, the nitric acid-treated LSCF electrode after annealing provided additional clarity on the surface chemistry modifications induced by chemical treatment. This step aimed to remove surface contaminants or modify surface functionalities, influencing the material's electrochemical properties and stability.

The peak fitting analysis, particularly focusing on Sr peaks, was pivotal in identifying any secondary phases or surface segregations that could affect the material's performance in electrochemical applications, such as solid oxide fuel cells (SOFCs) or oxygen separation membranes. These findings contribute to a comprehensive understanding of the material's surface chemistry evolution across various processing stages, facilitating the optimization of fabrication techniques to enhance device performance and longevity.

The X-ray photoelectron spectroscopy (XPS) analysis of the strontium (Sr) 3d spectrum reveals a characteristic doublet structure arising from the coupling of the $3d_{3/2}$ and $3d_{5/2}$ spin orbits. This doublet is a common feature in XPS spectra due to spin-orbit splitting, which occurs as a result of the interaction between the spin of the electron and its orbital angular momentum.

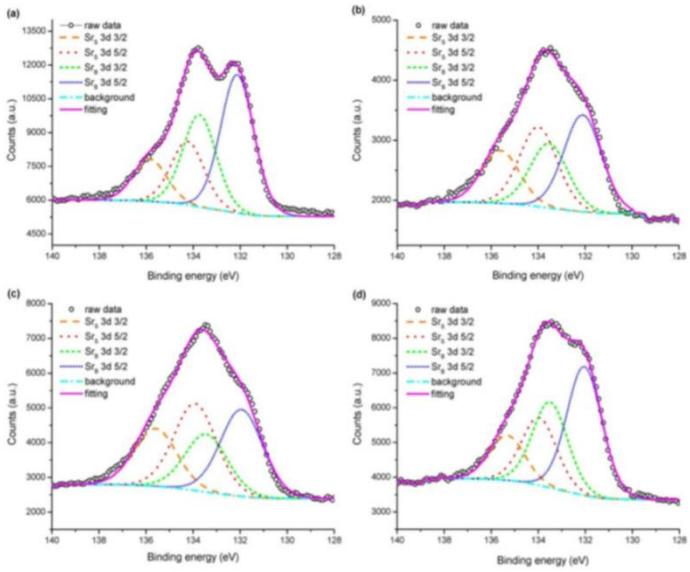

Figure 5: - Peak fitting results of Sr spectra for (a) raw LSCF powder, (b) freshly prepared LSCF electrode, (c) LSCF electrode after 24 h annealing, and (d) nitric acid-treated LSCF electrode after annealing.

During the peak fitting process of the Sr 3d spectrum, two distinct pairs of peaks corresponding to Sr $3d_{3/2}$ and Sr $3d_{5/2}$ spin orbits were identified. The pair with a lower binding energy was labeled as SrB, which typically corresponds to strontium atoms integrated within the bulk lattice structure of LSCF (lanthanum strontium cobalt ferrite). This suggests that these Sr atoms are part of the perovskite framework and are less influenced by surface interactions or

segregation effects.

Conversely, the pair denoted simply as Sr exhibited a higher binding energy, indicating that these Sr atoms are located at the surface of the LSCF electrode. Surface segregation or adsorption processes can lead to differences in binding energy compared to bulk-bound Sr atoms. The higher binding energy of the Sr peaks suggests that these surface Sr atoms may experience different local environments or bonding configurations compared to those within the bulk lattice. This surface-sensitive information is crucial for understanding the surface chemistry of LSCF electrodes and how it may influence their performance in electrochemical applications.

This detailed analysis provides valuable insights into the distribution and chemical state of Sr within LSCF electrodes, highlighting the importance of surface-sensitive techniques like XPS in studying material properties and optimizing their performance for applications such as solid oxide fuel cells (SOFCs) and oxygen separation membranes.

4. Conclusions

The objective of this project was to develop a novel oxygen separation tube using a perovskite as LSCF and a mixed ionic electronic conducting membrane oxide called SCN. The oxygen separation tube consists of a composite structure of a thick membrane layered on top of a porous body, together with a surface activation layer. The efficacy of extracting high-purity oxygen from compressed air using the obtained tube has been demonstrated. The accomplishment is credited to the practically perfect fabrication of a substantial membrane and gas seal between the tube and the metal flange. The separation behaviour demonstrated a trade-off correlation between the rate of permeation and the rate of oxygen collection, which can be attributed to the impact of airflow. The rate of permeation was 9 cm^3 min^(-1) cm^(-2) with a 20% rate of oxygen collection. The pure oxygen method, a novel evaluation technique, was also introduced here to determine the absolute permeability of the oxygen separation tube while disregarding the influence of airflow. The pure oxygen method proposes that the rate at which oxygen is separated follows the theoretical equation, assuming a process that is restricted by diffusion, even in thin parts of the membrane that are 50 μm thick. This discovery demonstrates that the presence of both the permeable structure and the activated surface layer enhances the surface response and is capable of enduring significant variations in pressure. The oxide ionic conductivity was measured by analysing the correlation between the permeation driving force and the observed permeation rate. At a temperature of 900 °C, the estimated ion conductivity was around 100 S/m, surpassing that of YSZ by two orders of magnitude and approaching the upper range of perovskite oxides documented in earlier studies. Moreover, the robustness and remarkable permeability of SCN were clearly observed when subjected to higher air pressures (20 atm), indicating its excellent stability in oxygen separation. Ultimately, the reliability of the oxygen separation tube was examined during a six-month duration, using air at a temperature of 900 °C and a pressure of 10 atm. The purity of the oxygen that was isolated was maintained at its original high level. On one hand, the pace of penetration decreased progressively. Analysis of the crystal structure of the tube employed in the extended experiment has shown that the consistent decrease in the rate of penetration is attributed to an interaction between SCN and Cr_2O_3 in the heat-resistant metal. Consequently,

it was anticipated that the oxygen separation tube that was created may be used for a long duration without any decline in quality by minimising the impact of chromium in the separation system.

Acknowledgements: Authors are grateful to National Institute of Technology Patna and Indian Institute of Technology Patna for their support in the experimental works.

Author contribution: Conceptualization, Data curation, Investigation, and Writing - original draft: Md. Adnan Iqbal. And Supervision, Writing - review and editing: A R Quaff.

Data availability: All data generated or analysed during this study are included in this published article.

Declarations

Ethical approval: Not applicable.

Conflict of interest: There is no interest conflict with others.

References

1. Wu, F., Argyle, M. D., Dellenback, P. A., & Fan, M. (2018). Progress in O2 separation for oxy-fuel combustion–A promising way for cost-effective CO2 capture: A review. Progress in Energy and Combustion Science, 67, 188-205.
2. Gür, T. M. (2022). Carbon dioxide emissions, capture, storage and utilization: Review of materials, processes and technologies. Progress in Energy and Combustion Science, 89, 100965.
3. Goren, A. Y., Erdemir, D., & Dincer, I. (2024). Comprehensive review and assessment of carbon capturing methods and technologies: An Environmental research. Environmental Research, 240, 117503.
4. Bahrun, M. H. V., Bono, A., Othman, N., & Zaini, M. A. A. (2022). Carbon dioxide removal from biogas through pressure swing adsorption–A review. Chemical Engineering Research and Design, 183, 285-306.
5. Liu, X., Cheng, S., Liu, H., Hu, S., Zhang, D., & Ning, H. (2012). A survey on gas sensing technology. Sensors, 12(7), 9635-9665.
6. Phair, J. W., & Badwal, S. P. S. (2006). Materials for separation membranes in hydrogen and oxygen production and future power generation. Science and technology of advanced materials, 7(8), 792.
7. Han, G. D., Choi, H. J., Bae, K., Choi, H. R., Jang, D. Y., & Shim, J. H. (2017). Fabrication of lanthanum strontium cobalt ferrite–gadolinium-doped ceria composite cathodes using a low-price inkjet printer. ACS applied materials & interfaces, 9(45), 39347-39356.
8. Schlenz, H., Baumann, S., Meulenberg, W. A., & Guillon, O. (2022). The development of new perovskite-type oxygen transport membranes using machine learning. Crystals, 12(7), 947.
9. Zhang, J., Zhang, Z., Chen, Y., Xu, X., Zhou, C., Yang, G., ... & Shao, Z. (2018). Materials design for ceramic oxygen permeation membranes: Single perovskite vs. single/double perovskite composite, a case study of tungsten-doped barium strontium cobalt ferrite. Journal of membrane science, 566, 278-287.
10. Hu, D., Wang, T., Ma, Q., Liu, X., Shang, L., Li, D., ... & Wang, R. (2019). Effect of inclusions on low cycle fatigue lifetime in a powder metallurgy nickel-based superalloy FGH96. International Journal of Fatigue, 118, 237-248.

11. Hu, J., Zhang, T., Zhang, Q., Yan, X., Zhao, S., Dang, J., & Wang, W. (2021). Application of calcium oxide/ferric oxide composite oxygen carrier for corn straw chemical looping gasification. Bioresource Technology, 330, 125011.
12. Ma, W., He, X., Wang, W., Xie, S., Zhang, Q., & Wang, Y. (2021). Electrocatalytic reduction of CO 2 and CO to multi-carbon compounds over Cu-based catalysts. Chemical Society Reviews, 50(23), 12897-12914.
13. Motuzas, J., Liu, S., & da Costa, J. C. D. (2022). Thermal Swing Reduction-Oxidation of Me (Ba, Ca, or Mg) SrCoCu Perovskites for Oxygen Separation from Air. Processes, 10(11), 2239.
14. Thebo, K. H., Qian, X., Wei, Q., Zhang, Q., Cheng, H. M., & Ren, W. (2018). Reduced graphene oxide/metal oxide nanoparticles composite membranes for highly efficient molecular separation. Journal of materials science & technology, 34(9), 1481-1486.
15. Chandio, I., Janjhi, F. A., Memon, A. A., Memon, S., Ali, Z., Thebo, K. H., ... & Khan, W. S. (2021). Ultrafast ionic and molecular sieving through graphene oxide based composite membranes. Desalination, 500, 114848.
16. Dey, M., Katabathuni, R. V., Badgayan, N. D., & Sahu, S. K. (2022, January). Finite Element Analysis of High-Density Polyethylene (HDPE) Nanocomposite for Potential Use as Dental Implant. In International Conference on Advances in Mechanical Engineering and Material Science (pp. 229-236). Singapore: Springer Nature Singapore.
17. Song, J., Wang, Z., Tan, X., Cui, Y., Kawi, S., & Liu, S. (2021). Simultaneous hydrogen and oxygen permeation through BaCe0. 70Fe0. 10Sc0. 20O3-δ perovskite hollow fiber membranes. Journal of Membrane Science, 635, 119513.
18. Fischer, L., Ran, K., Schmidt, C., Neuhaus, K., Baumann, S., Behr, P., ... & Meulenberg, W. A. (2023). Role of Fe/Co Ratio in Dual Phase Ce0. 8Gd0. 2O2− δ–Fe3− xCoxO4 Composites for Oxygen Separation. Membranes, 13(5), 482.
19. Sunarso, J., Hashim, S. S., Zhu, N., & Zhou, W. (2017). Perovskite oxides applications in high temperature oxygen separation, solid oxide fuel cell and membrane reactor: A review. Progress in Energy and Combustion Science, 61, 57-77.
20. Zhang, Z., Zhou, W., Wang, T., Gu, Z., Zhu, Y., Liu, Z., ... & Jin, W. (2023). Ion–Conducting Ceramic Membrane Reactors for the Conversion of Chemicals. Membranes, 13(7), 621.